Airborne Doppler Lidar Investigation of Sea Surface Reflectance at a 355-nm Ultraviolet Wavelength

ZHIGANG LI

Deutsches Zentrum für Luft- und Raumfahrt, Institut für Physik der Atmosphäre, Oberpfaffenhofen, Germany, and Key Laboratory of Ocean Remote Sensing, Ministry of Education of China, Ocean University of China, Qingdao, China

CHRISTIAN LEMMERZ, ULRIKE PAFFRATH, OLIVER REITEBUCH, AND BENJAMIN WITSCHAS

Deutsches Zentrum für Luft- und Raumfahrt, Institut für Physik der Atmosphäre, Oberpfaffenhofen, Germany

(Manuscript received 3 March 2009, in final form 25 August 2009)

ABSTRACT

The analysis of the sea surface reflectance for different incidence angles based on observations of an airborne Doppler lidar at an ultraviolet wavelength of 355 nm is described. The results were compared to sea surface reflectance models, including the contribution from whitecaps, specular reflection, and the subsurface volume backscattering. The observations show the expected effect of the wind stress on the sea surface reflectance and allow new insights into the significant contribution from subsurface reflectance for large incidence angles. While most of the observations and model results were obtained for isotropic reflectance, first results on anisotropic reflectance are also provided. The results from this study are relevant to future spaceborne wind lidar instruments, for example, the Atmospheric Dynamics Mission (ADM)-Aeolus, which could use the sea surface reflectance for the calibration of intensity and wind.

1. Introduction

The wind-driven sea surface waves with the combination of capillary and capillary–gravity waves, the influence of wind on the whitecaps coverage of sea surface, and the uncertainty of subsurface water volume backscattering, motivated a study on sea surface reflectance. For Fresnel optical reflection on the sea surface, the relation between the sea wave slope variance and sea surface wind speed (SSW) was studied over several decades, such as by Cox and Munk (1954), Wu (1972, 1990), and Hu et al. (2008). They developed different models for sea wave slope variance for the simulation of the optical reflection at sea surface. Optical remote sensing with lidar (light detection and ranging) was applied for analysis of laser backscattering from the sea surface. Bufton et al. (1983) reported airborne measurement of laser backscatter from sea surface using laser wavelengths at 337 nm, 532 nm, and 9.5 μm, and comparisons were made with model predictions up to 15° off-nadir angle. Menzies et al. (1998) described the sea surface reflectance and the link to surface wind speed with observations from the space-based Lidar In-Space Technology Experiment (LITE), and provided expressions for a sea surface reflectance model. The measurements at wavelengths of 1064, 532, and 355 nm were used for the analysis of sea surface reflectance: the 1064-nm data could be fitted well with the model curves; the 532- and 355-nm channels showed a large difference for large off-nadir angles due to the neglected subsurface backscattering in the models and the limited signal dynamic range of 10^2 for the lidar detection. Tratt et al. (2002) performed the first airborne Doppler lidar investigation of the wind-modulated sea surface angular retroreflectance signature; the anisotropic retroreflectance behavior of sea surface was studied at an infrared (IR) wavelength of 10.6 μm.

The sea surface reflectance models can be studied and validated by the use of spaceborne and airborne lidar instrument. The spaceborne lidar backscatter measurements on the Cloud-Aerosol Lidar and Infrared

Corresponding author address: Zhigang Li, Key Laboratory of Ocean Remote Sensing, Ministry of Education of China, Ocean University of China, 266003, Qingdao, China.
E-mail: lizg.ouc@gmail.com

DOI: 10.1175/2009JTECHA1302.1

Pathfinder Satellite Observations (CALIPSO) were used to derive the SSW from the relation between SSW and sea wave slope variance (Hu et al. 2008). The Atmosphere Dynamics Mission (ADM)-Aeolus of the European Space Agency (ESA 2008) will be the first Doppler wind lidar mission in space. This study will contribute to the consolidation of the sea surface reflectance model for ultraviolet (UV) wavelengths for different incidence angles and SSW. The sea surface reflectance signal is used for calibration of the satellite instrument when nadir-pointing. The sea surface return might be used for obtaining a zero-wind reference in addition to land surface returns in wind-measurement mode with incidence angles of 37.6°, in order to compensate for errors in the knowledge of the satellite platform attitude and speed (zero-wind calibration).

The subsurface backscattering should be taken into account at visible and UV wavelengths, because of its more significant contribution relatively to IR wavelengths. In the past, only a few experiments have been done for the validation of sea surface reflectance, especially for visible and UV wavelengths under different incidence angles. The Atmospheric Laser Doppler Instrument (ALADIN) Airborne Demonstrator (A2D), operating at a UV wavelength of 355 nm, was developed by the Deutsches Zentrum für Luft- und Raumfahrt (DLR), and the first test flights were performed in October 2005. The A2D is the airborne prototype for the instrument ALADIN on ADM-Aeolus. The observations of sea surface reflectance for different off-nadir angles used for this study were obtained during the airborne campaigns in 2007 and 2008.

The A2D system and the airborne campaigns are described briefly in section 2. Section 3 contains a discussion of all the contributions to the sea surface reflectance models. Section 4 describes the observations of the sea surface return from the A2D airborne campaigns and the comparison with the sea surface reflectance models. Finally, conclusions and an outlook are presented in section 5.

2. Lidar description and airborne campaign

The lidar instrument ALADIN on ADM-Aeolus is developed to measure vertical profiles of one wind component within the troposphere and lower stratosphere with high accuracy (ESA 2008). A new technique, combining an aerosol Mie and a molecular Rayleigh receiver to benefit from their complementarities in vertical coverage, is used by ALADIN. The main system parameters of the airborne prototype of ALADIN—the A2D—are listed in Table 1.

TABLE 1. Instrument parameters of the A2D.

Laser transmitter	
Laser type	Diode-pumped, frequency-tripled, injection-seeded Nd:YAG
Laser pulse energy	55–65 mJ
Laser pulse repetition rate	50 Hz
Laser wavelength	354.9 nm
Laser line width	45 MHz FWHM
Laser beam divergence	80–90 μrad ($\pm 3\sigma$; 99.7%)
Laser beam diameter	16 mm (99.7%)
Telescope and receiver	
Telescope	0.2-m-diameter Cassegrain telescope
Receiver FOV	100 μrad
Receiver	Fizeau interferometer for Mie receiver
	Fabry–Perot interferometer for Rayleigh receiver
ACCD	0.85 quantum efficiency
	16 × 16 pixels in image zone
	25 range bins
Platform	
Aircraft	DLR Falcon 20
Flight altitude	8–12 km
Slant angle	20° off-nadir
LOS range resolution	315 m

The objective of the airborne and ground campaigns with the A2D is to validate the predicted instrument and wind measurement performance and to establish a dataset of atmospheric observations for the validation and improvement of retrieval algorithms (Durand et al. 2006; Reitebuch et al. 2008, 2009; Paffrath et al. 2009). The ground return, including land and sea surface, was obtained during airborne campaigns in 2007 and 2008. Due to the similarity in signal spectrum for aerosol backscattering and ground return, the ground return signal can be extracted from the Mie receiver with a Fizeau interferometer by summing all detectors pixels containing ground return signal. Normally, when the aircraft follows a straight flight track, the instrument is pointing at an angle of 20° off-nadir downward to measure the line-of-sight (LOS) velocity (LOSV). Thus, by rolling the aircraft about 20°, an off-nadir angle of around 3° for the LOS can be achieved (the residual 3° off-nadir angle results from the pitch angle of the aircraft); by rolling the aircraft about −17.5°, an off-nadir angle of around 37.5° for the LOS can be achieved, which is close to the off-nadir angle of the satellite instrument LOS (Fig. 1). In this way, the relation of relative sea surface backscattering intensity and the angle of incidence can be analyzed. The beam footprint at sea surface depends on the beam divergence, flight altitude, and off-nadir angle, and values are

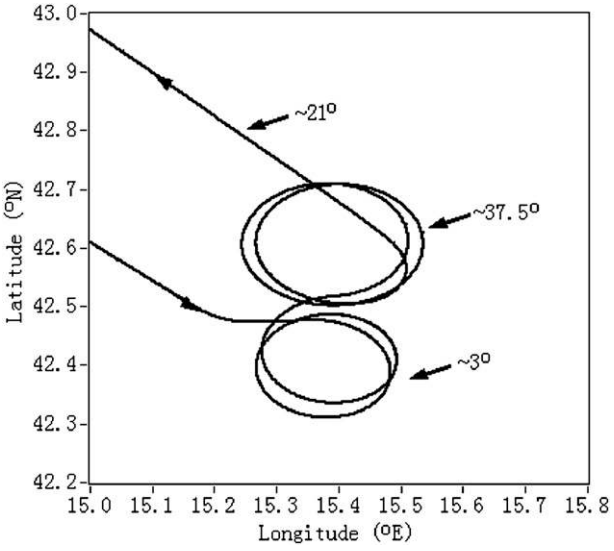

FIG. 1. Example of flight track over the Adriatic Sea on 28 Nov 2007, the first curve with ~3° off-nadir angle, the following curves with ~37.5° off-nadir angle, and the straight flight with ~21° off-nadir angle.

between 0.7 and 0.9 m for off-nadir angles of 3°–37.5°. Table 2 summarizes the A2D observations used for this study from an airborne campaign in November 2007 and in December 2008 on the DLR Falcon aircraft.

Accumulation charge coupled devices (ACCDs) are used as detectors with a high quantum efficiency of 85% and low noise, which improves signal-to-noise ratio (SNR) for the sea surface return, especially for the weak signals at a large off-nadir angle. The dynamic range of the ACCD is 6×10^5, which is sufficient for the expected several-orders-of-magnitude dynamic range of the sea surface return for nadir and off-nadir angles up to 37.5°.

Observations with sea surface return for different off-nadir angles from four flights were analyzed, and the corresponding nearby locations and flight altitudes are provided in Table 2. An example of a track with circle flights resulting in different off-nadir angles is shown in Fig. 1. Each circle track has a duration of ~4 min and a radius of ~10 km.

3. Sea surface reflectance models

The total sea surface reflectance can be divided into three contributions: the backscattering of whitecaps on the sea surface (Koepke 1984), the specular reflectance of the sea surface (Barrick 1968), and the light backscattered by the subsurface (Morel and Prieur 1977; Morel 1980; Gordon and Morel 1983). The total reflectance can be written as (Menzies et al. 1998)

$$R = R_{\mathrm{wc}} + (1 - W)R_s + (1 - R_{\mathrm{wc}})R_U, \qquad (1)$$

TABLE 2. Airborne sea surface observations.

Location	Lat, lon (nearby circle)	Time (UTC)	Date	Flight altitude (km)
Balearic Sea	42.25°N, 5.10°E	~1530	17 Nov 2007	9.03
Baltic Sea	54.35°N, 12.25°E	~1415	19 Nov 2007	7.96
Adriatic Sea	42.50°N, 15.40°E	~1500	8 Nov 2007	8.92
North Sea	54.50°N, 3.50°E	~1430	17 Dec 2008	7.40

where R is the total sea surface reflectance; the first component R_{wc} is the reflectance of the whitecaps; the second component $(1 - \mathrm{W})R_s$ is the specular reflectance from areas that are not covered by whitecaps, where R_s is the Fresnel specular reflectance, and W is the relative area covered by whitecaps; the third component $(1 - R_{\mathrm{wc}})R_U$ is the contribution from the volume backscattering of the water molecules and suspended materials in the water, where R_U is the equivalent subsurface reflectance. The third component is based on the assumption that the reflectance of whitecaps is the same for incident light coming from above or under the surface, thus reducing the underwater reflectance by the factor $(1 - R_{\mathrm{wc}})$. The details for the three contributions are described below.

a. Whitecaps contribution

The effective reflectance of the whitecaps $R_{\mathrm{wc,eff}}$ on the sea surface and the fraction of the surface coverage W describe the optical reflectance of whitecaps R_{wc}. The effective reflectance is found to be 22% in the visible spectral range by Koepke (1984), and we assume that there is no significant difference for a wavelength of 355 nm. The reflectance of the whitecaps is proportional to coverage of whitecaps W.

Several statistical studies describe W as a function of wind speed U measured at 10 m above the sea surface (Monahan and O'Muircheartaigh 1980, 1986). Estimates of the fractional coverage of whitecaps have been carried out previously by photographic methods, either from space or from a stationary platform above the ocean surface. Monahan and O'Muircheartaigh (1980) summarized the relationship between W and U, which has been validated for wind velocities between 4 and 25 m s^{-1}:

$$W = 2.95 \times 10^{-6} U^{3.52}. \qquad (2)$$

The fact that the coverage of whitecaps is related to the atmospheric stability was shown by Monahan and O'Muircheartaigh (1986), and a reanalysis of data including the atmospheric stability yielded

$$W = 1.95 \times 10^{-5} U^{2.55} \exp(-0.0861 \Delta T), \qquad (3)$$

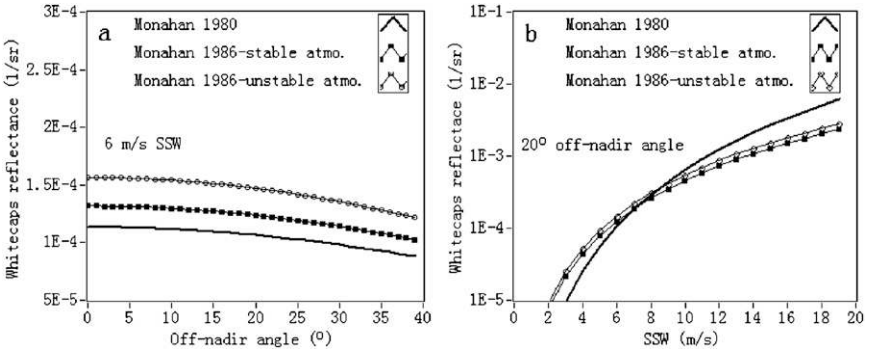

FIG. 2. Comparison of whitecaps reflectance under different fractional coverage conditions ($\Delta T = 0$ K and $\Delta T = -2$ K are considered for the stable and unstable situations, respectively): (a) whitecaps reflectance for 6 m s^{-1} SSW for different off-nadir angles; (b) whitecaps reflectance for 20° off-nadir angle and different SSW.

where $\Delta T = T_a - T_w$ represents the temperature difference between the air T_a and the water T_w; ΔT is a measure of the atmospheric stability, where $\Delta T = 0$ K indicates a stable atmosphere.

The backscattering of whitecaps can be treated as a Lambertian reflector, which appears equally bright in all directions when illuminated. When the geometry is off-nadir, the reflectance is depending on the off-nadir angle θ and can be written as

$$R_{\mathrm{wc}} = \frac{WR_{\mathrm{wc,eff}}\cos(\theta)}{\pi}. \tag{4}$$

The atmospheric stability could not be derived from the airborne observations. Thus, for all comparisons between simulations and observation, Eq. (3) is used with $\Delta T = 0$ K (stable atmosphere). Figure 2 illustrates the difference in whitecaps reflectance for an unstable condition with $\Delta T = -2$ K, which results in a factor of 1.19 higher reflectance. For unstable atmospheric conditions the whitecap contribution will rise exponentially, which is significant for high wind speed conditions. An effective reflectance of 22% and the fractional coverage depending on wind speed for stable situation (Eq. 3) are used for the analysis in this paper.

It should be mentioned that the laser beam footprint of ~1 m is rather small, and the whitecaps could be not adequately sampled. The error should be limited because of the low contribution from whitecaps explicitly for the low SSW, which results in a contribution of below 10^{-3} sr^{-1}.

b. Specular reflectance

The wave facet of capillary and capillary–gravity waves at surface directly affects light reflectance by the sea surface, which is described by the wave slope variance. Cox and Munk (1954) expressed a linear relationship between wind speed U at 12.5 m above sea surface and the variance σ^2 of the slope distribution, which was calculated from measurements of the bidirectional sea surface reflectance pattern of reflected sunlight. It is assumed that the slope distribution is a Gaussian function with a variance σ^2:

$$\sigma^2 = 0.003 + 0.005\,12U_{12.5\mathrm{m}}. \tag{5}$$

This relation is based on the assumption of an isotropic contribution (i.e., azimuthally averaged). Cox and Munk (1954) also described different slope variances for upwind–downwind σ_u^2 and crosswind σ_c^2 situations:

$$\begin{aligned}\sigma_u^2 &= 0.003\,16U_{12.5\mathrm{m}},\\ \sigma_c^2 &= 0.003 + 0.001\,92U_{12.5\mathrm{m}}.\end{aligned} \tag{6}$$

In the following, we use the wind speed U at 10 m above the sea surface instead of 12.5 m. Wu (1990) reanalyzed the data of Cox and Munk (1954) by using a two-branch logarithmic fit; the equations are expressed as

$$\begin{aligned}\sigma^2 &= 0.0276\,\log_{10}U + 0.009 \quad (U < 7\ \mathrm{m\ s^{-1}}),\\ \sigma^2 &= 0.138\,\log_{10}U - 0.084 \quad (U \geq 7\ \mathrm{m\ s^{-1}}).\end{aligned} \tag{7}$$

When the wind speed is less than 7 m s^{-1}, capillary waves are the predominant component of wind-driven waves. When wind speed exceeds 7 m s^{-1}, the surface becomes rougher and gravity waves become more important (Wu 1990).

The relation between SSW and wave slope variance was assessed by Hu et al. (2008) on a global scale using the collocated wind speed measurements from the Advanced Microwave Scanning Radiometer–Earth

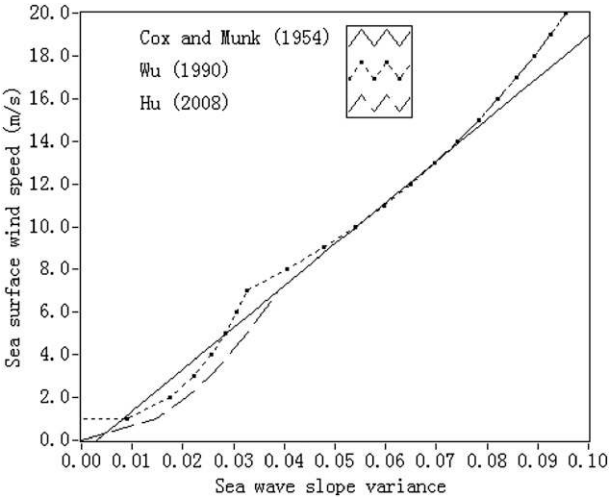

FIG. 3. Relations between SSW and sea surface wave slope variance σ^2 from previous studies: the Cox and Munk (1954) model has a linear relation; the Wu (1990) model is logarithmic with two branches; and the Hu et al. (2008) model is a combined curve with three branches.

Observing System (AMSR-E) and the wave slope variance derived from the sea surface integrated backscatter of the CALIPSO lidar:

$$\begin{aligned}
&\sigma^2 = 0.0146\sqrt{U} && (U < 7\ \mathrm{m\ s^{-1}}),\\
&\sigma^2 = 0.003 + 0.005\,12U && (13.3\ \mathrm{m\ s^{-1}} > U \geq 7\ \mathrm{m\ s^{-1}}),\\
&\sigma^2 = 0.138\log_{10}U - 0.084 && (U \geq 13.3\ \mathrm{m\ s^{-1}}).
\end{aligned} \tag{8}$$

Although the recent analysis by Hu et al. (2008) is based on a more comprehensive global sampling with the use of a spaceborne lidar, we adopt the linear relationship of the model of Cox and Munk (1954) in this paper to describe the wave slope variance of the sea surface because of the anisotropic situation present. Also, the three different types of relation between SSW and wave slope variance show good consistency for SSW up to 20 m s^{-1}, which is illustrated in Fig. 3.

The specular reflectance R_s of the sea surface is expressed as (Menzies et al. 1998)

$$R_s = \frac{\rho}{2\pi\sigma^2\cos^4(\theta)}\exp\left[-\frac{\tan^2(\theta)}{\sigma^2}\right], \tag{9}$$

where ρ is the Fresnel reflectance. It is derived from the refractive index of seawater, and $\rho = 0.0219$ is used for the wavelength at 355 nm. Figure 4 shows the simulation results of the sea surface specular reflectance depending on the off-nadir angles and the SSW with a very low contribution for large off-nadir angles.

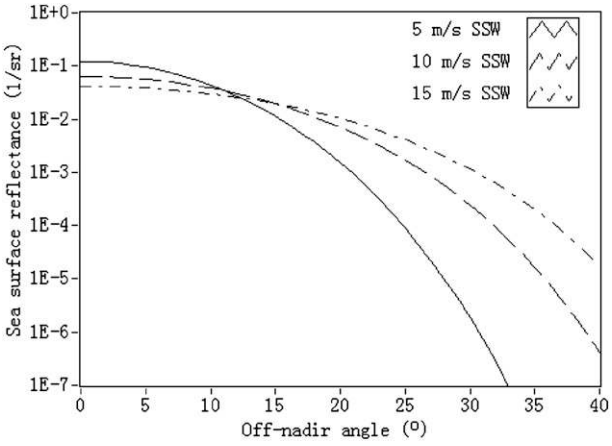

FIG. 4. Sea surface specular reflectance for different off-nadir angles and SSW at 355 nm.

The anisotropic reflectance behavior is described in the following form (Tratt et al. 2002):

$$R_s' = \frac{\rho}{4\pi\sigma_u\sigma_c\cos^4(\theta)}\exp\left[-\frac{\tan^2(\theta)}{2\sigma'^2(\phi)}\right], \tag{10}$$

where σ'^2 is the azimuth-dependent wave slope variance estimated according to

$$\sigma'^2(\phi) = \frac{\sigma_u^2\sigma_c^2}{\sigma_c^2\cos^2(\phi) + \sigma_u^2\sin^2(\phi)}, \tag{11}$$

where ϕ is the angle subtended by the direction of wind flow and the lidar viewing azimuth.

c. Subsurface contribution

Backscattered radiation from the water volume should be considered to predict the sea surface reflectance for UV and visible laser wavelengths, but it is negligible for longer wavelengths because of the strong absorption in water. However, it is difficult to describe this contribution, because of the uncertainty of the seawater optical properties. Normally, the water column backscatter is handled as Lambertian backscatter (Gordon and Morel 1983) in general cases, and a parameter R_0, which is called the equivalent subsurface reflectance, is defined to describe the subsurface backscattering as subsurface irradiance at zero depth (located just below the surface). The subsurface R_U reflectance can be written as

$$R_U = \frac{R_0\cos(\theta)}{\pi}. \tag{12}$$

A popular expression of R_0 is shown in Eq. (13), which was derived by both Morel and Prieur (1977) and Whitlock et al. (1982):

$$R_0 = f^0 \frac{b_b(\lambda)}{a(\lambda) + b_b(\lambda)}, \tag{13}$$

where f^0 is the proportionality factor for irradiance reflectance based on the geometry of the incoming light and the volume scattering in water. The inherent optical properties of the water are described by the volume absorption coefficient $\alpha(\lambda)$ and the backscattering coefficient $b_b(\lambda)$. The expression is valid for infinitely deep water, where the only contributor to the reflected signal is the water body rather than the ocean floor. For open ocean with clean water a constant proportionality factor $f^0 = 0.33$ is commonly used and is sufficient for many applications (Tyler et al. 1972; Albert 2003). A value of $R_0 = 0.0088$ is used for UV wavelengths for clean ocean water according to Bufton et al. (1983), where also values for $a = 0.32\ \mathrm{m}^{-1}$ and $b_b = 0.017\ \mathrm{m}^{-1}$ are provided, which result in a factor-of-2 higher value for R_0 when using Eq. (13) and $f^0 = 0.33$. The variation of the ocean turbidity will determine the value of R_0, within a range from 0.008 to 0.02 (Morel and Prieur 1977). The turbidity of the water was not determined from the airborne observations, and thus a value for clean ocean water of $R_0 = 0.0088$ was chosen for the model simulations. The SSW shows very weak influence on this term, and the error is below 1% when the SSW influence is neglected, which was calculated using an analytical model by Albert (2003).

Thus, the full description of the sea surface reflectance model, including the off-nadir angle θ, and the terms W and σ^2 depending on the SSW according to Eqs. (3) and (5), is expressed as

$$R(\theta) = \frac{WR_{\mathrm{wc,eff}}\cos(\theta)}{\pi} + \frac{(1-W)\rho}{2\pi\sigma^2\cos^4(\theta)}\exp\left[-\frac{\tan^2(\theta)}{\sigma^2}\right] + (1 - R_{\mathrm{wc}})\frac{R_0\cos(\theta)}{\pi}. \tag{14}$$

Figure 5 shows the sea surface reflectance resulting from the model of Eq. (14) for different SSW and different incidence angles. Two situations, with and without subsurface contribution, are considered. The difference is very small for off-nadir angles below 10°, but it becomes noticeable when the off-nadir angle is larger than 15°. For off-nadir angles larger than 30°, the contribution of specular reflectance is very low, but the contribution from the subsurface plays a dominant role and results in a contribution that does not depend on SSW. The sea surface reflectance for low SSW and off-nadir angles larger than 30° is nearly two orders higher when the subsurface contribution is taken into account.

For large off-nadir angles, the contribution from subsurface reflectance will dominate when the SSW is low,

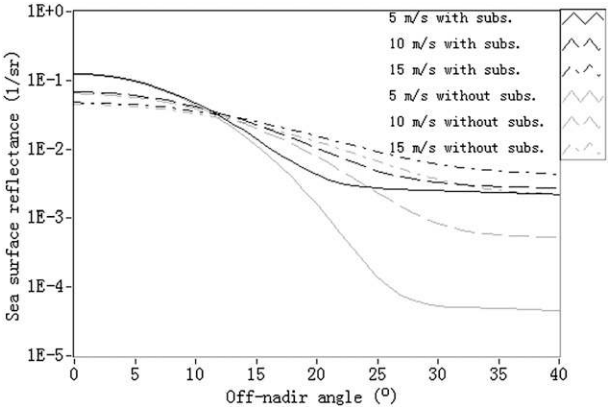

FIG. 5. Simulation of total sea surface reflectance for 5, 10, and 15 m s^{-1} SSW with considering subsurface contribution (subs., black lines) and without considering subsurface contribution (gray lines).

and the error mainly arises from the uncertainty in R_0. The contribution from whitecaps reflectance will play an important role, when the SSW increases and the temperature difference between water and atmosphere increases, leading to unstable conditions. The errors in the simulations of the whitecaps reflectance arise mainly from the unknown atmospheric stability and the error in the effective reflectance provided by Koepke (1984) with (22 ± 11)%. The error from the specular reflectance is low due to its small contribution to the overall reflectance for large off-nadir angles. For an SSW of 10 m s^{-1}, the contribution of specular reflectance is lower than 10^{-3} sr^{-1} for off-nadir angles larger than 30°. Thus, the error from the specular reflectance is lower than 15%. The sea surface reflectance model is analyzed for UV wavelengths using airborne lidar observations for difference incidence angles in the following.

4. Field experiments data analysis

a. Data analysis

Airborne observations with the A2D from different flights were used for this study according to Table 2. The raw data from the ACCD detector contains the signal of a number of $P = 20$ accumulated laser pulses. The sea surface return can be regarded as the combination of Lambertian reflection and mirror specular reflection. It shows a similar small-frequency bandwidth as the outgoing laser pulse or aerosol signal and can be well detected by the Fizeau interferometer of the Mie receiver. Figure 6 shows an example of the measured signal intensity from one range gate of the Mie ACCD for $P = 20$, in which the sea surface return for three different off-nadir angles is clearly separated. The sea surface return

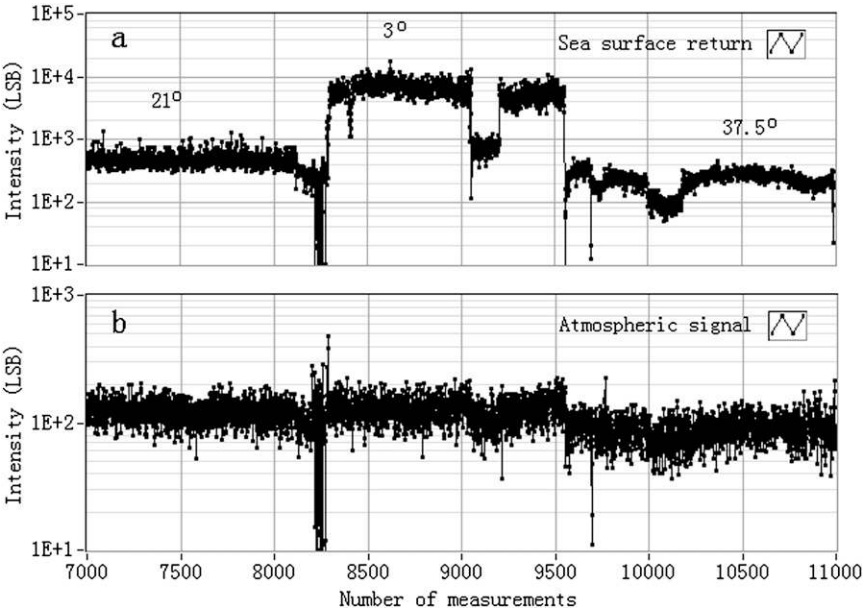

FIG. 6. (a) The Mie ACCD signal intensity for $P = 20$ [in least-significant bit (LSB) units] of the sea surface return and (b) the atmospheric signal above the sea surface with 20 accumulated laser pulses and 315-m range resolution for different off-nadir angles from airborne observations with the A2D on 28 Nov 2007.

at large off-nadir angles of 37.5° is much weaker compared to lower off-nadir angles and is close to the atmospheric signal above the sea surface.

The first step in the analysisis the determination of the range gate in which the sea surface is located. The gradient of intensity shows almost no height dependency for a clear atmosphere without clouds, except close to the lidar instrument, but shows high values for the sea surface return. The range gate of sea surface return can be determined by setting threshold levels on the gradient signal to extract the upper and lower boundaries. Usually, the sea surface return is contained in one range gate.

The highest temporal resolution of the ACCD is 2.1 μs, which corresponds to 315-m range gates. Because of the 315-m range resolution, the contamination of atmospheric signal in the range gate of the sea surface return for the weak signals at large off-nadir angles cannot be neglected. The range r_0 from the aircraft to the sea surface is determined from the flight altitude and off-nadir angle. The range r_1 is the distance of the aircraft to the lower boundary of the range gate of the sea surface return and is calculated by using the commanded range resolution for the ACCD. The portion of the atmospheric signal in the range gate of the sea surface return with a 315-m range resolution is $(r_1 - r_0)/315$. The corrected intensity for the sea surface return I_{SSR} is calculated by subtracting the range-square corrected atmospheric signal of the range gate above the sea surface return from the total intensity of the sea surface return I'_{SSR}:

$$I_{SSR} = I'_{SSR} - \frac{r^2_{ato} I'_{ato}}{r^2_{SSR}} \frac{(r_1 - r_0)}{315}, \tag{15}$$

where I'_{ato} is the intensity of the atmospheric signal of the range gate above sea surface return, and r^2_{ato} and r^2_{SSR} are the detection ranges of the atmospheric signal and the sea surface return.

The sea surface return was obtained during weather conditions of clear sky with no or low cloud cover. Raw data with a temporal resolution of 0.4 s ($P = 20$) are averaged over 2 min (~½ circle flight for 3° and 37.5° off-nadir angles) in order to improve the SNR of the sea surface return and are used to derive the sea surface return intensity. The sea surface return for different off-nadir angles is detected at different ranges; thus the ratio of the sea surface return and the atmospheric signal of the range gate above the sea surface return is used as a relative intensity for normalization. This method assumes temporal and horizontal spatial homogenous aerosol distribution above the sea surface in the area of the circle flights (10–50 km). With this method, the influence of differences in extinction for different ranges can be eliminated, but the relative intensity becomes weighted by the backscatter coefficient of aerosol above the sea surface. From the airborne measurements with

the A2D it is not possible to derive an absolute, calibrated value for R in units of sr^{-1}, because of the lack of radiometric calibration on land surface targets as performed by Tratt et al. (2002). The method of the signal normalization to stratospheric altitudes with no aerosol as applied for CALIPSO and LITE observations (Hu et al. 2008; Menzies et al. 1998) does not work properly because of the low flight altitude of 8–12 km. As the main purpose was to study the reflectance under different incidence angles, no absolute calibration of the lidar signal was necessary. For the comparison, the ratio of observations for different off-nadir angles θ_1 and θ_2 is used to derive the SSW used in the model. The SSW is derived from minimization of the difference of the observation compared to the simulated sea surface reflectance according to

$$\left[\frac{r_I(\theta_1)}{r_I(\theta_2)} - \frac{R(\theta_1, \mathrm{SSW})}{R(\theta_2, \mathrm{SSW})}\right] = \mathrm{Minimum}, \qquad (16)$$

where r_I is the observed intensity ratio of the sea surface return I_{SSR} and the atmospheric signal I'_{ato}. The off-nadir angles of 3° and 21° are normally used in the analysis in this paper. All airborne observations of the same day are multiplied by a factor f for normalization according to Eq. (17):

$$\sum_{i=1}^{n} \frac{f r_I(\theta_i) - R(\theta_i, \mathrm{SSW})}{R(\theta_i, \mathrm{SSW})} = 0, \qquad (17)$$

where θ_i is the off-nadir angle of observation i. The relative intensity is related to the aerosol influence above the sea surface. The factor f is used to normalize the relative intensity $r_I(\theta_i)$ by comparison with reflectance $R(\theta_i, \mathrm{SSW})$.

b. Discussion of results

Sea surface returns over the Balearic Sea were obtained during a flight on 17 November 2007 with off-nadir angles of 3° and 21°. While the aircraft was rolling, 12 observations with 0.4-s temporal resolution can be used for analysis. Figure 7 shows the comparison between the sea surface reflectance from the calculated relative intensity for different off-nadir angles and model curves for SSW from 12 to 15 m s^{-1}. The lidar observations are averaged over 2 min for 3° and 21° off-nadir angles, and they match the model curve for an SSW of 12 m s^{-1}. The lidar observations with ~0.4 s follow the model curves with a large variation due to their low SNR. A wind speed of about 10 m s^{-1} was obtained by the scatterometer on QuikSCAT (Fig. 12; Callahan 2006), but with a difference of about 3 h between the lidar observation and QuikSCAT.

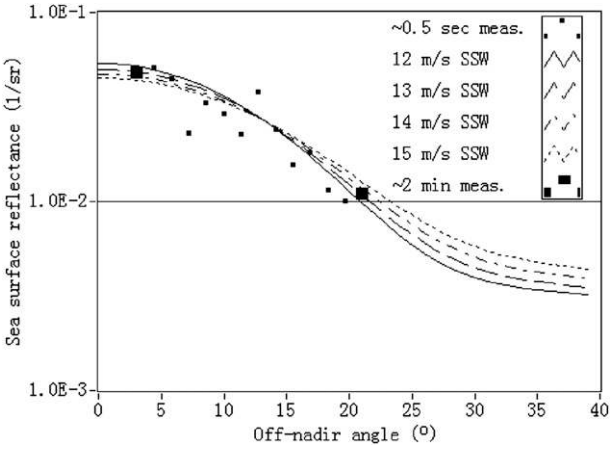

FIG. 7. Sea surface reflectance at 355 nm from observations on 17 Nov 2007 over the Balearic Sea (black dots); model curves are shown for SSW from 12 to 15 m s^{-1}.

The flights on 19 and 28 November were performed over the Baltic and Adriatic Seas, and Figs. 8 and 9 show the lidar observations of the sea surface reflectance and the simulated model curves. The three observations for different off-nadir angles follow the model curves for 5–6 and 6–7 m s^{-1} SSW on 19 and 28 November, respectively. The dispersion of observations with low SNR obtained with a temporal resolution of ~0.4 s in Fig. 7 and Fig. 9 also indicates the azimuthal dependency of sea surface reflectance model. A small difference at 37.5° off-nadir angle is observed for both days due to the uncertainty of subsurface reflectance contribution in the model and the error from the aerosol correction in

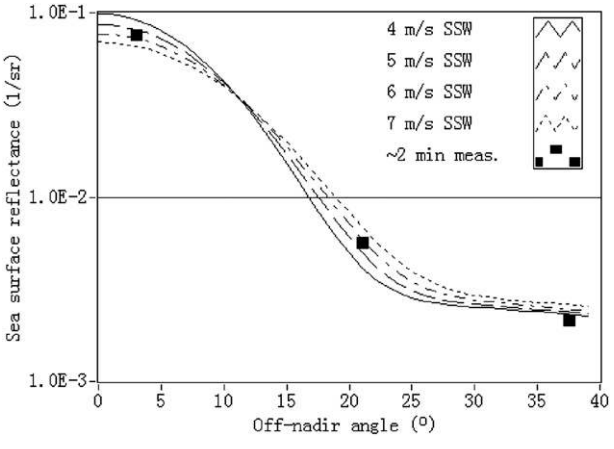

FIG. 8. Sea surface reflectance at 355 nm from observations on 19 Nov 2007 over the Baltic Sea (black dots); model curves are shown for SSW from 4 to 7 m s^{-1}.

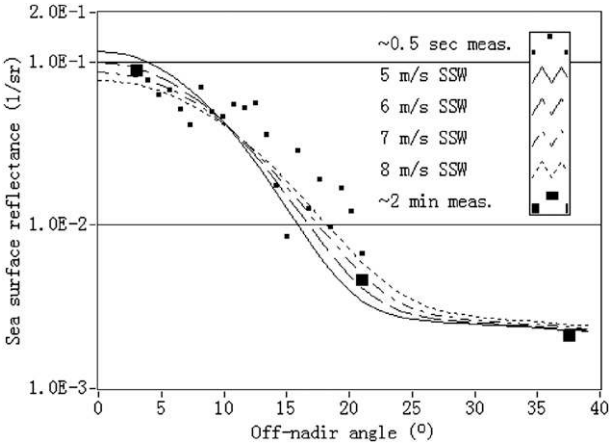

FIG. 9. Sea surface reflectance at 355 nm from observations on 28 Nov 2007 over the Adriatic Sea (black dots); model curves are shown for SSW from 5 to 8 m s^{-1}.

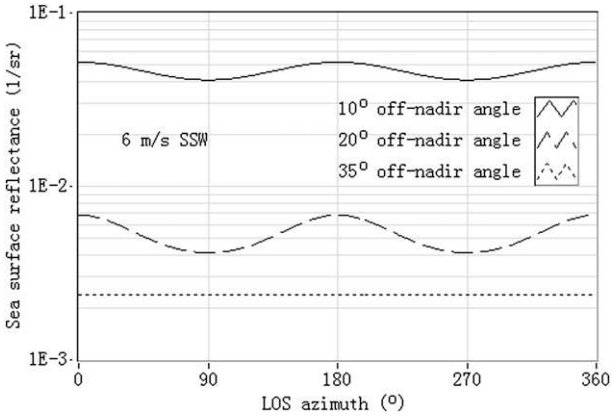

FIG. 10. Dependence of the sea surface reflectance from azimuth angle with an SSW of 6 m s^{-1} and off-nadir angles of 10°, 20°, and 35°.

the range gate of sea surface return in Eq. (15). The measured SSW by QuikSCAT indicates a SSW of about 5 m s^{-1} with a 2-h time difference for both days.

The mean isotropic wave slope variance of Cox and Munk (1954) model is used for simulations; however, sea surface angular reflectance is modulated by the wind as confirmed by Tratt et al. (2002). So the wind direction and anisotropic reflectance behavior should be considered. Figure 10 shows the dependence of the sea surface reflectance from azimuth angle with a SSW of 6 m s^{-1} and off-nadir angles of 10°, 20°, and 35° according to Eq. (10) and Eq. (11). The sea surface reflectance varies by a factor of 1.75 for differences in azimuth angle of 90° for off-nadir angles of 20°, while it is almost constant for large off-nadir angles of 35°.

The slope distribution for observations at 3° and 37.5° off-nadir angles is closer to a mean slope variance than for the 21° off-nadir angle. The 3° off-nadir observations are obtained within a circle flight as the average value of upwind and crosswind wave slope variance, while the 21° off-nadir observations are obtained from a straight flight. Figure 11 shows the model and observation results for 17 December 2008, with three types of slope variance: upwind–downwind, isotropic, and crosswind. Five observations at different off-nadir angles are analyzed, and the derived SSW is around 15 m s^{-1}. This is higher than the SSW of around 10 m s^{-1} from the National Aeronautics and Space Administration (NASA) Quick Scatterometer (QuikSCAT), which was obtained with a time difference of 4 h (Fig. 12). The observation at 20° deviates from the isotropic model because of wind-modulated sea surface angular reflectance, as the crosswind situation is obtained from the LOS direction of the lidar and the wind direction from QuikSCAT. The error bars with ±25% atmospheric signal correction are included for the observations at 31° and 36° off-nadir angles, because of the uncertainty of the portion of the atmospheric signal in the range gate of sea surface return.

For the observations at a large off-nadir angle of 37.5°, the sea surface reflectance is about 2.1×10^{-3} sr^{-1} for an SSW of around 5 m s^{-1} for both days (Figs. 8, 9). The contribution from the whitecaps is approximately 1×10^{-4} sr^{-1}, and the contribution from the specular reflectance can be neglected at these large off-nadir angles (Fig. 4). Thus, the total reflectance is almost dominated by the subsurface backscattering. The estimated value of R_0 is obtained by comparing the observation with the model for a large off-nadir angle of 37.5°. The calculated subsurface backscatter R_0 is about 0.83% for both days, compared to a value of 0.88% provided by

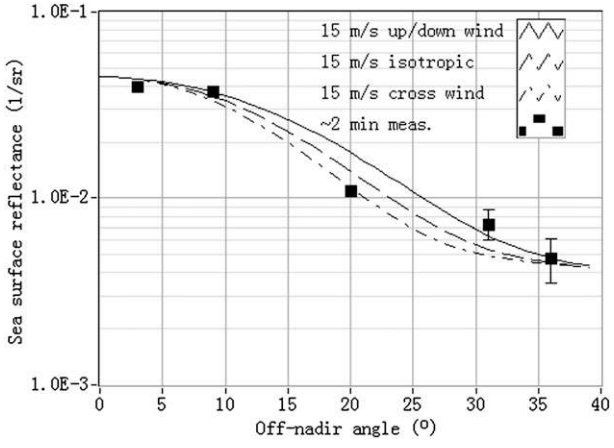

FIG. 11. Sea surface reflectance at 355 nm from observations on 17 Dec 2008 over the North Sea (black dots); isotropic and anisotropic model curves are shown for SSW of 15 m s^{-1}.

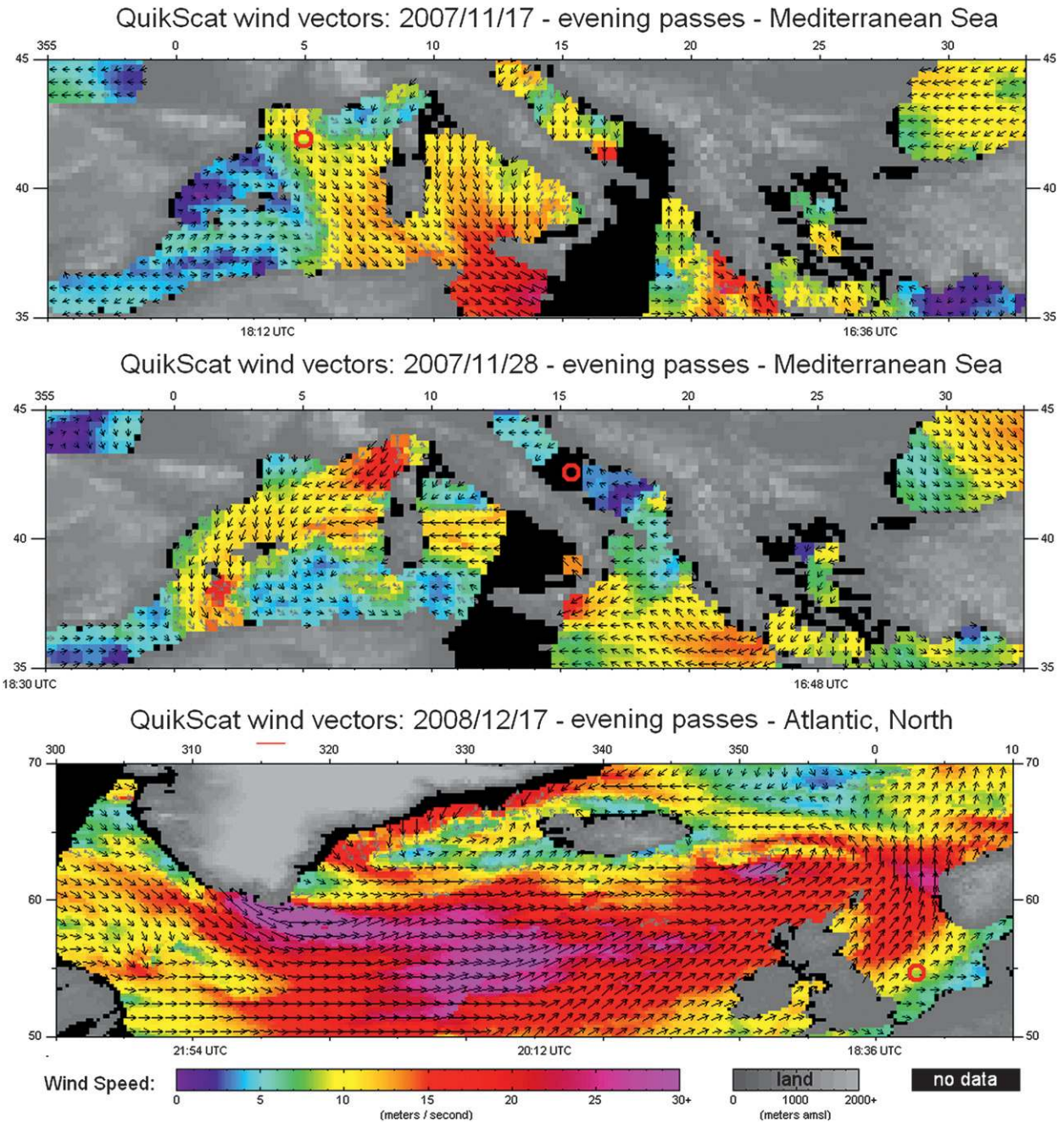

FIG. 12. Wind vector and speed (color coded) derived from QuikSCAT on (top) 17 Nov 2007, (middle) 28 Nov 2007, and (bottom) 17 Dec 2008; the red circles indicate the location of the airborne lidar observation. The QuikSCAT figures are provided online at http://www.remss.com/qscat/qscat_browse.html.

Bufton et al. (1983). Without considering the subsurface reflectance, the total reflectance at 37.5° would be a factor of 50 lower for an SSW of 5 m s^{-1}. Menzies et al. (1998) estimated a value of 1%–1.5% as the equivalent Lambertian reflectance from the subsurface scattering at a wavelength of 532 nm from observations in the Gulf of California. The calculated value in this paper is lower because of the slightly higher water absorption at the wavelength of 355 nm.

The SSW only slightly influences the subsurface reflectance, which can be treated as constant for identical off-nadir angles and seawater conditions. The whitecaps contribution will change to the predominant part when the SSW increases, which can be seen when comparing

Figs. 7 and 11 (high wind speed) to Figs. 8 and 9 (low wind speed) for large off-nadir angles.

5. Summary and conclusions

The observations of an airborne Doppler lidar at a wavelength of 355 nm under different off-nadir angles are used for this study of the sea surface reflectance for the first time. The sea surface reflectance models, including contribution from whitecaps and specular reflections, are described in detail. The contribution from subsurface backscatter plays a significant role for incidence angles higher than 15°. Without considering the contribution from the volume backscattering of the water column, the simulated reflectance would be a factor of 50 for incidence angles of 35°–40° and an SSW of 5 m s^{-1}. Previous measurements at UV wavelengths with the space-based lidar LITE were limited by the dynamic range of the receiver and the signal noise level to sea surface backscatter of 10^{-2} sr and off-nadir angles of about 15° (Menzies et al. 1998). Within this study, airborne lidar measurements in the UV up to almost 40° off-nadir angles with sufficient signal levels were presented for low to medium SSW (5–15 m s^{-1}). Thus, it could be validated that the subsurface backscatter plays a significant role for incidence angles higher than 15° for UV wavelengths of 355 nm. This complements the results obtained by Menzies et al. (1998) for subsurface volume backscattering at the visible wavelength of 532 nm.

The subsurface equivalent reflectance R_0 in the models is difficult to estimate because of the uncertainty of the inherent optical properties of water. The derived value of R_0 from observations at a wavelength of 355 nm over the Baltic and Adriatic Seas is about 0.83%, which is close to the value of 0.88% provided by Bufton et al. (1983). Because of the large off-nadir angles of 37.5° of the observations, the contributions from specular reflectance and whitecaps can be neglected for low SSW.

The isotropic reflectance could be derived from observations during circle flights of the aircraft while the anisotropic reflectance was observed during straight flights with a constant off-nadir-pointing angle of the lidar. Both the isotropic and anisotropic reflectance show good consistency between observations and simulations. Further observations of the anisotropic reflectance characteristics are needed to consolidate these first results.

The results from this study are relevant to future spaceborne wind lidar missions, such as the Atmospheric Dynamics Mission (ADM)-Aeolus. The sea surface reflectance could be used for calibration of intensity and zero-wind with the instruments pointing at large off-nadir angles in the wind measurement mode (e.g., 37.6° for ADM-Aeolus) and during nadir pointing in response calibration modes. For spaceborne wind lidar missions, which will use high off-nadir angles and UV wavelengths, the subsurface reflectance becomes important compared to the whitecaps and specular reflectance. Further studies have to analyze the influence of the effect of the sea surface movement on the retrieved wind speed of the Doppler lidar instrument for different off-nadir angles.

Acknowledgments. The airborne campaigns were funded by the European Space Agency (ESA) and the Deutsches Zentrum für Luft- und Raumfahrt (DLR). The grant for Z. G. Li for his stay at DLR from February 2008 to May 2009 was provided by the China Scholarship Council (CSC).

REFERENCES

Albert, A., 2003: An analytical model for subsurface irradiance and remote sensing reflectance in deep and shallow case-2 waters. *Opt. Exp.,* **11,** 2873–2890.

Barrick, D. E., 1968: Rough surface scattering based on the specular point theory. *IEEE Trans. Antennas Propag.,* **16,** 449–454.

Bufton, J. L., F. E. Hoge, and R. N. Swift, 1983: Airborne measurements of laser backscatter from the ocean surface. *Appl. Opt.,* **22,** 2603–2618.

Callahan, P. S., 2006: QuikSCAT science data product user's manual: Overview and geophysical data products. Jet Propulsion Laboratory, V3.0, D-18053-RevA, 85 pp.

Cox, C., and W. Munk, 1954: Measurement of the roughness of the sea surface from photography of the sun's glitter. *J. Opt. Soc. Amer.,* **44,** 838–850.

Durand, Y., E. Chinal, M. Endemann, R. Meynart, O. Reitebuch, and R. Treichel, 2006: ALADIN airborne demonstrator: A Doppler wind lidar to prepare ESA's Aeolus Explorer mission. *Proc. SPIE Opt. Photon.,* **6296,** 13–17.

ESA, 2008: ADM-Aeolus Science Rep. SP-1311. ESA Communication Production Office, 121 pp.

Gordon, H. R., and A. Y. Morel, 1983: *Remote Assessment of Ocean Color for Interpretation of Satellite Visible Imagery: A Review*. Springer-Verlag, 114 pp.

Hu, Y., and Coauthors, 2008: Sea surface wind speed estimation from space-based lidar measurements. *Atmos. Chem. Phys.,* **8,** 3593–3601.

Koepke, P., 1984: Effective reflectance of oceanic whitecaps. *Appl. Opt.,* **23,** 1816–1824.

Menzies, R. T., D. M. Tratt, and W. H. Hunt, 1998: Lidar in-space technology experiment measurements of sea surface directional reflectance and the link to surface wind speed. *Appl. Opt.,* **37,** 5550–5559.

Monahan, E. C., and I. O'Muircheartaigh, 1980: Optimal power-law description of oceanic whitecap coverage dependence on wind speed. *J. Phys. Oceanogr.,* **10,** 2094–2099.

——, and ——, 1986: Whitecaps and the passive remote sensing of the ocean surface. *Int. J. Remote Sens.,* **7,** 627–642.

Morel, A., 1980: In-water and remote measurements of ocean color. *Bound.-Layer Meteor.,* **18,** 177–201.

——, and L. Prieur, 1977: Analysis of variations in ocean color. *Limnol. Oceanogr.,* **22,** 709–722.

Paffrath, U., Ch. Lemmerz, O. Reitebuch, B. Witschas, I. Leike, and V. Freudenthaler, 2009: The airborne demonstrator for the direct-detection Doppler wind lidar ALADIN on ADM-Aeolus. Part II: Simulations and Rayleigh receiver radiometric performance. *J. Atmos. Oceanic Technol.,* **26,** 2516–2530.

Reitebuch, O., and Coauthors, 2008: Pre-launch validation of ADM-Aeolus with an airborne direct-detection wind lidar. *Proc. 24th Int. Laser Radar Conf.,* Boulder, CO, ICLAS, 41–44.

——, C. Lemmerz, E. Nagel, U. Paffrath, Y. Durand, M. Endemann, F. Fabre, and M. Chaloupy, 2009: The airborne demonstrator for the direct-detection Doppler wind lidar ALADIN on ADM-Aeolus. Part I: Instrument design and comparison to satellite instrument. *J. Atmos. Oceanic Technol.,* **26,** 2501–2515.

Tratt, D. M., R. T. Menzies, M. P. Chiao, D. R. Cutten, J. Rothermel, R. M. Hardesty, J. N. Howell, and S. L. Durden, 2002: Airborne Doppler lidar investigation of the wind-modulated sea-surface angular retroreflectance signature. *Appl. Opt.,* **33,** 6941–6950.

Tyler, J. E., R. C. Smith, and W. H. Wilson, 1972: Predicted optical properties for clear natural water. *J. Opt. Soc. Amer.,* **62,** 83–90.

Whitlock, H., D. S. Bartlett, and E. A. Gurganus, 1982: Sea foam reflectance and influence on optimum wavelength for remote sensing of ocean aerosols. *Geophys. Res. Lett.,* **9,** 719–722.

Wu, J., 1972: Sea-surface slope and equilibrium wind-wave spectra. *Phys. Fluids,* **13,** 741–747.

——, 1990: Mean square slopes of the wind-disturbed water surface, their magnitude, directionality, and composition. *Radio Sci.,* **25,** 37–48.